A dual-energy subtraction technique for microcalcification imaging in digital mammography—A signal-to-noise analysis

Michael R. Lemacks,[a] S. Cheenu Kappadath,[b] Chris C. Shaw, Xinming Liu, and Gary J. Whitman
Department of Imaging Physics, University of Texas M. D. Anderson Cancer Center, Houston, Texas 77030

(Received 13 December 2001; accepted for publication 26 May 2002; published 18 July 2002)

Breast cancer may manifest as microcalcifications (μCs) in x-ray mammography. However, the detection and visualization of μCs are often obscured by the overlapping tissue structures. The dual-energy subtraction imaging technique offers an alternative approach for imaging and visualizing μCs. With this technique, separate high- and low-energy images are acquired and their differences are used to ''cancel'' out the background tissue structures. However, the subtraction process could increase the statistical noise level relative to the calcification contrast. Therefore, a key issue with the dual-energy subtraction imaging technique is to weigh the benefit of removing the cluttered background tissue structure over the drawback of reduced signal-to-noise ratio in the subtracted μC images. In this report, a theoretical framework for calculating the (quantum) noise in the subtraction images is developed and the numerical computations are described. We estimate the noise levels in the dual-energy subtraction signals under various imaging conditions, including the x-ray spectra, μC size, tissue composition, and breast thickness. The selection of imaging parameters is optimized to evaluate the feasibility of using a dual-energy subtraction technique for the improved detection and visualization of μCs. We present the results and discuss its dependence on imaging parameters.
[DOI: 10.1118/1.1494832]

Key words: dual-energy subtraction imaging, digital mammography, microcalcifications, signal-to-noise ratio

I. INTRODUCTION

Screening and diagnosis in x-ray mammography rely on the detection and visualization of microcalcifications (μCs) and/or soft tissue masses. The early detection of breast cancer has been shown to decrease breast cancer mortality.[1] The μCs are composed mainly of calcium with attenuation properties greater than that of soft tissue. The detection and visualization of μCs are relatively easy over a uniform tissue background, but limited by the ''clutter'' due to overlapping tissue background present on the mammogram. The clutter in tissue background arises from the structures of glandular tissue, ducts, vessels, and soft tissue masses in the breast. Depending upon the degree of clutter, the contrast of μCs, and the manner of overlap, it may be difficult to detect a μC, even though there may be sufficient contrast-to-noise ratio (CNR).

Dual-energy subtraction imaging techniques[2–9] offer an alternative approach to the detection and visualization of μCs. With this technique, high- and low-energy images are separately acquired and ''subtracted'' from each other in a weighted fashion to cancel out the cluttered tissue structure so as to decrease the obscurity from overlapping tissue structures. Early work on theoretical optimization of dual-energy mammography together with experimental results were done using a prototype digital scanned projection radiography system (septaless ionization chamber).[2,3] These works first demonstrated the application of dual-energy imaging to mammography. However, the applicability of their results were somewhat limited since the theoretical optimization was done for monoenergetic x-ray beams and the initial experimental results were acquired by using radiographic x-ray beams (50 and 115 kVp). An ideal observer receiver operating characteristic study with computer-simulated dual-exposure mammographic images based on monoenergetic x rays showed that dual-energy images could produce calcium images with higher sensitivity and specificity.[6] Dual-energy mammography with computed radiography- (CR) based systems have also been investigated.[4,5,7,8] In single-exposure CR techniques, where the cassette consists of two storage phosphors plates separated by a filter, numerical calculations have been used to optimize the front (low-energy) and rear (high-energy) phosphor plates.[4,5] Dual-energy mammography has also been successfully demonstrated experimentally with dual-exposure CR techniques.[7,8] Although dual-exposure CR techniques could provide clinically useful information, it was prone to motion-induced artifacts[7] and yielded a lower sensitivity to small calcifications[8] compared to traditional single-energy mammography.

Nevertheless, dual-energy mammography has been shown to be a promising technique to suppress structure background in mammographic imaging. However, due to subtraction processing in dual-energy mammography, the calcification CNR in the subtraction images tends to be lower than that in the unsubtracted images.[9] The calcification CNR in the subtraction images depends on the choice of x-ray spectra and other imaging parameters, in addition to the signal-to-noise ratio

(SNR) in the original (unsubtracted) images. Therefore, the key issue in dual-energy subtraction imaging is to weigh the benefit of removing the cluttered background against the drawback of reduced calcification CNR in the subtraction images.

In this paper, a theoretical framework for calculating the calcification CNR in dual-energy images is developed. For a fixed entrance exposure, we study the influence of the various imaging parameters (polyenergetic x-ray spectrum, scintillating material, μC size, tissue composition, and breast thickness) on the calcification CNR. While previous numerical studies[2,6] have performed optimizations for monoenergetic x-ray beams, our calculations are based on polyenergetic (mammographic) spectra and incorporate clinically relevant imaging parameters. Our aim in this study was to evaluate and optimize the dual-energy technique when standard clinical practices and practical considerations are maintained. In order to preserve generality of the results and isolate the effects of system-dependent components, we consider only the propagation of quantum (Poisson) noise from the original (unsubtracted) images to the subtraction images. The methods used for computing the calcification CNR are described. Results of the numerical computations are presented and used to demonstrate and discuss the feasibility of using a dual-energy subtraction imaging technique to improve the detection and visualization of μCs with mammography.

II. THEORY

In this section, the formalism for dual-energy subtraction (calcification) imaging is presented. Within this framework, the calcification CNR in the subtraction image is derived for use in the numerical studies. Although the derived framework can be used for situations with both quantum and system noise, only the quantum (Poisson) noise is considered in the present numerical study.

A. Two-energy versus three-energy subtraction

In mammography, one can assume that there are three attenuating materials in the breast: adipose tissue, glandular tissue, and calcifications (only sparsely present). Ideally, it would be best to use images acquired at three separate energies to estimate the thicknesses of the three attenuating materials.[10] However, compared to dual-energy subtraction imaging, three-energy subtraction imaging leads to an additional reduction of image SNR, which would potentially require higher patient exposure, increased time to complete the exam (which could lead to motion artifacts), and more complicated subtraction image processing. Mammography differs from other radiographic procedures in that the breast is compressed to a largely uniform thickness (that can be easily measured). With the total breast thickness known, the task of three-material composition measurement can be reduced to that of two materials.[9] Dual-energy imaging can also be used to estimate the total breast thickness in an uncompressed part of the breast (the sum of the adipose tissue and glandular tissue thicknesses assuming no calcifications are present).[11]

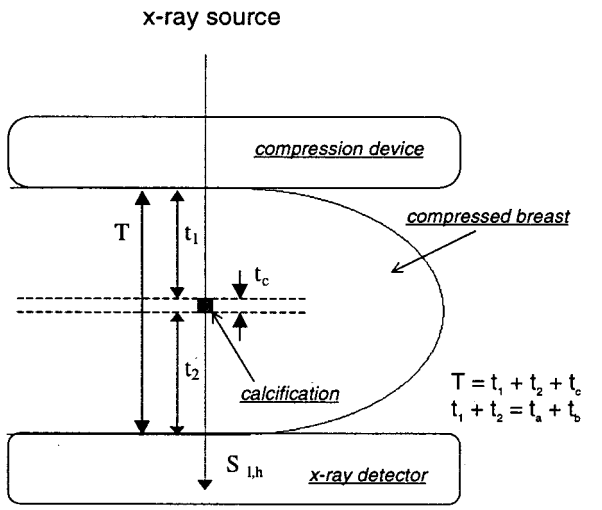

FIG. 1. A compressed breast of thickness T, with a cubic μC of dimension, t_c, and adipose and glandular tissues of thickness t_a and t_b, respectively, where $t_a+t_b=t_1+t_2$.

B. Dual-energy microcalcification imaging technique

Assume that along the x-ray path, a compressed breast is composed of adipose tissue of thickness t_a, glandular tissue of thickness t_b, and a μC of thickness t_c (Fig. 1). The total breast tissue thickness, T (cm) is given by

$$T=t_a+t_b+t_c. \tag{1}$$

Assuming that polyenergetic x rays are used, the mean measured signals in the low- and high-energy images, S_l and S_h, can be expressed as

$$S_j=\int dE\cdot R_j\cdot d^2\cdot\Phi_j(E)\cdot e^{-\mu_a(E)t_a-\mu_b(E)t_b-\mu_c(E)t_c}\cdot A(E)\cdot Q(E);\quad j=l,h, \tag{2}$$

where, R_l and R_h are the unattenuated low- and high-energy x-ray exposures in (C/kg) at the detector plane, d is the pixel size in centimeters (cm), $\Phi_l(E)$ and $\Phi_h(E)$ are the unattenuated low- and high-energy photon fluence per unit exposure per unit energy (photons/cm^2 keV C/kg) at the detector input, $A(E)$ is the photon absorption ratio of the detector as a function of photon energy E(keV), and $Q(E)$ is the detector response function and represents the signal generated by each detected x-ray photon (i.e., gain) as a function of photon energy E(keV). The energy-dependent linear-attenuation coefficients (1/cm) for adipose tissue, glandular tissue, and calcifications are given by $\mu_a(E)$, $\mu_b(E)$, and $\mu_c(E)$, respectively.

Defining $\Delta\mu_b(E)\equiv\mu_b(E)-\mu_a(E)$ and $\Delta\mu_c(E)\equiv\mu_c(E)-\mu_a(E)$, referred to as the difference-attenuation coefficients and solving for t_a in Eq. (1), the low- and high-energy image signals, Eq. (2) can be rewritten as

$$S_j = \int dE \cdot R_j \cdot d^2 \cdot \Phi_j(E) \cdot e^{-\mu_a(E)T} \cdot e^{-\Delta\mu_b(E)t_b - \Delta\mu_c(E)t_c} \cdot A(E) \cdot Q(E); \quad j = l,h. \tag{3}$$

Analogous to the optical density, we define x-ray densities for the low- and high-energy images, D_l and D_h, as follows:

$$D_j \equiv \ln\left(\frac{S_j^0}{S_j}\right); \quad j = l,h, \tag{4}$$

where S_j^0 is the unattenuated reference signal obtained by imaging without the breast present. Using the signals attenuated by 100% adipose tissue, as the low- and high-energy reference signals, the modified x-ray densities, D_l' and D_h' (now functions of only the glandular tissue thickness, t_b, and calcification thickness, t_c) can be defined as

$$D_j' = F_j(t_b,t_c) \equiv \ln\left(\frac{S_j^a}{S_j}\right); \quad j = l,h. \tag{5}$$

Substituting Eq. (3) into Eq. (5), D_l' and D_h' can be expressed as follows:

$$D_j' = \ln\left(\frac{\int dE \cdot R_j \cdot d^2 \cdot \Phi_j(E) \cdot e^{-\mu_a(E)T} \cdot A(E) \cdot Q(E)}{\int dE \cdot R_j \cdot d^2 \cdot \Phi_j(E) \cdot e^{-\mu_a(E)T} \cdot e^{-\Delta\mu_b(E)t_b - \Delta\mu_c(E)t_c} \cdot A(E) \cdot Q(E)}\right); \quad j = l,h. \tag{6}$$

The main task of dual-energy subtraction imaging is to determine the mapping functions for glandular tissue thickness, $t_b = f_b(D_l', D_h')$, and calcification thickness, $t_c = f_c(D_l', D_h')$, from the measured x-ray densities (images), $D_l' = F_l(t_b,t_c)$ and $D_h' = F_h(t_b,t_c)$. Typically, the form of the mapping functions, f_b and f_c, can be determined by interpolation of calibration measurements. The mapping functions vary with $\Phi_j(E), T, A(E)$, and $Q(E)$, hence the calibrations must be performed for different x-ray techniques, breast thicknesses, absorption ratios, and detector response functions.

C. The special case of monoenergetic x-ray images

Since the x-ray spectra used in diagnostic imaging are polyenergetic, Eq. (6) cannot be solved analytically for t_b and t_c. The use of monoenergetic x rays allows the inverse functions f_b and f_c to be analytically solved. We will therefore demonstrate the reduction of the three-material/energy imaging problem into to a dual-material/energy imaging problem with the use of monoenergetic x-ray sources.

Recall that our model for the breast consists of adipose tissue of thickness t_a, glandular tissue of thickness t_b, and a μC of thickness t_c (Fig. 1). If p_l^0 and p_l are defined as the unattenuated and attenuated signals from the low-energy monoenergetic spectrum, and p_h^0 and p_h are defined as the unattenuated and attenuated signals from the high-energy spectrum, the x-ray densities D_l and D_h defined in Eq. (4) can be expressed as

$$D_j \equiv \ln(p_j^0/p_j) = \mu_{aj}T + (\mu_{bj} - \mu_{aj})t_b + (\mu_{cj} - \mu_{aj})t_c; \quad j = l,h, \tag{7}$$

where, μ_{ij} $(i = b,c;\ j = l,h)$ are the linear attenuation coefficients for glandular tissue $(i = b)$ and μC $(i = c)$, at low $(j = l)$ and high $(j = h)$ energies, respectively. Similarly, the modified x-ray densities, D_l' and D_h' defined in Eq. (5), can be expressed, using Eq. (7), as follows:

$$D_j' \equiv \ln(p_j^a/p_j) = D_j - \ln(p_j^0/p_j) = \Delta\mu_{bj}\,t_b + \Delta\mu_{cj}\,t_c; \quad j = l,h, \tag{8}$$

where $\Delta\mu_{bj} = \mu_{bj} - \mu_{aj}$, $\Delta\mu_{cj} = \mu_{cj} - \mu_{aj}$, and p_l^a and p_h^a are the low- and high-energy reference signals corresponding to attenuation by 100% adipose tissue. Rearranging Eq. (8) into matrix form, we get

$$\begin{pmatrix} D_l' \\ D_h' \end{pmatrix} = \begin{pmatrix} \Delta\mu_{bl} & \Delta\mu_{cl} \\ \Delta\mu_{bh} & \Delta\mu_{ch} \end{pmatrix} \begin{pmatrix} t_b \\ t_c \end{pmatrix}. \tag{9}$$

Equation (9) represents two linear equations with two unknowns whose solutions are easily derived. The mapping functions for glandular tissue thickness (f_b) and calcification thickness (f_c) can be analytically expressed as functions of the difference attenuation coefficients $(\Delta\mu_{ij})$ and x-ray densities (D_l' and D_h') as follows:

$$t_b = f_b(D_l', D_h') = \frac{\Delta\mu_{ch}D_l' - \Delta\mu_{cl}D_h'}{\Delta\mu_{bl}\Delta\mu_{ch} - \Delta\mu_{cl}\Delta\mu_{bh}}, \tag{10}$$

and

$$t_c = f_c(D_l', D_h') = \frac{\Delta\mu_{bl}D_h' - \Delta\mu_{bh}D_l'}{\Delta\mu_{bl}\Delta\mu_{ch} - \Delta\mu_{cl}\Delta\mu_{bh}}. \tag{11}$$

D. Noise and SNR in poly-energetic images

The noise level in the x-ray densities D_l and D_h can be related to the SNR in the low- and high-energy raw images as follows:

$$\sigma_{D_j'}^2 = \left(\frac{\partial D_j'}{\partial S_j}\right)^2 \sigma_{S_j}^2 = \left(\frac{1}{S_j}\right)^2 \sigma_{S_j}^2 = \frac{1}{\mathrm{SNR}_{S_j}^2}; \quad j = l,h, \tag{12}$$

where we assume that S_l^0 and S_h^0 can be measured with high precision and therefore contribute little to the noise terms in Eq. (12). In Eq. (3), the signal contribution from photons with an energy between E and $E + dE$ is proportional to the mean number of photons detected within that energy interval $[\overline{n}(E)dE = dE \cdot R_j \cdot d^2 \cdot \Phi_j(E) \cdot e^{-\mu_a(E)T} \cdot e^{-\Delta\mu_b(E)t_b - \Delta\mu_c(E)t_c}$

$\cdot A(E)$], multiplied by the signal generated by each absorbed x-ray photon [the gain factor $=Q(E)$]. Characteristic of the x-ray detection process, $n(E)dE$, the number of detected photons between E and $E+dE$ is a stochastic quantity governed by Poisson statistics. Thus, the variance of the $n(E)dE$ is equal to its mean value, $\overline{n}(E)dE$. Furthermore, since $\overline{n}(E)dE$ is typically large in diagnostic x-ray imaging, it can be assumed to fluctuate with a Gaussian distribution. Strictly speaking, the gain factor $Q(E)$, is also a stochastic quantity. However, its contribution to the signal variance can be ignored when the number of scintillated photons generated for each absorbed x-ray photon is reasonably large (e.g., cesium iodide scintillators yield ~1250 optical photons for a 25 keV x-ray photon). Since the number of absorbed x rays are subject to an average gain of $Q(E)$, the noise variance for the energy interval of E to $E+dE$ can be approximated by $Q^2(E)\overline{n}(E)dE$.[12,13] Summing the variances over all energy intervals, the total noise variances in the low- and high-energy image signals, $\sigma^2_{S_j}(j=l,h)$, can be expressed as

$$\sigma^2_{S_j}=\int dE\cdot R_j\cdot d^2\cdot \Phi_j(E)\cdot e^{-\mu_a(E)T}\cdot e^{-\Delta\mu_b(E)t_b-\Delta\mu_c(E)t_c}\cdot A(E)\cdot Q^2(E). \tag{13}$$

The SNR in the low- and high-energy images are

$$\mathrm{SNR}_{S_j}=\frac{\int dE\cdot R_j\cdot d^2\cdot \Phi_j(E)\cdot e^{-\mu_a(E)T}\cdot e^{-\Delta\mu_b(E)t_b-\Delta\mu_c(E)t_c}\cdot A(E)\cdot Q(E)}{\left(\int dE\cdot R_j\cdot d^2\cdot \Phi_j(E)\cdot e^{-\mu_a(E)T}\cdot e^{-\Delta\mu_b(E)t_b-\Delta\mu_c(E)t_c}\cdot A(E)\cdot Q^2(E)\right)^{1/2}}. \tag{14}$$

E. Noise and SNR in subtracted images

The variations of D'_l and D'_h can be expressed as

$$dD'_j=\left(\frac{\partial D'_j}{\partial t_b}\right)dt_b+\left(\frac{\partial D'_j}{\partial t_c}\right)dt_c;\quad j=l,h. \tag{15}$$

The variations dD'_l and dD'_h are linear combinations of the variations dt_b and dt_c. The parameters $\partial D'_j/\partial t_i\,(i=b,c;j=l,h)$ can be explicitly derived using Eq. (6) as

$$\left(\frac{\partial D'_j}{\partial t_i}\right)=\left(\frac{\int dE\cdot R_j\cdot d^2\cdot \Phi_j(E)\cdot e^{-\mu_a(E)T}\cdot \Delta\mu_i(E)\cdot e^{-\Delta\mu_b(E)t_b-\Delta\mu_c(E)t_c}\cdot A(E)\cdot Q(E)}{\int dE\cdot R_j\cdot d^2\cdot \Phi_j(E)\cdot e^{-\mu_a(E)T}\cdot e^{-\Delta\mu_b(E)t_b-\Delta\mu_c(E)t_c}\cdot A(E)\cdot Q(E)}\right). \tag{16}$$

Equation (16) shows that $\partial D'_j/\partial t_i$ can be interpreted as the $\Delta\mu_{ij}(E)$ averaged over the detected energy spectrum, thus, $\partial D'_j/\partial t_i$ can be represented as $\overline{\Delta\mu_{ij}}\,(i=b,c;j=l,h)$. The pair of equations described in Eq. (15) can be expressed in matrix form as

$$\begin{pmatrix} dD'_l \\ dD'_h \end{pmatrix}=\begin{pmatrix} \overline{\Delta\mu}_{bl} & \overline{\Delta\mu}_{cl} \\ \overline{\Delta\mu}_{bh} & \overline{\Delta\mu}_{ch} \end{pmatrix}\begin{pmatrix} dt_b \\ dt_c \end{pmatrix}. \tag{17}$$

Solving for dt_b and dt_c yields

$$\begin{pmatrix} dt_b \\ dt_c \end{pmatrix}=\begin{pmatrix} \overline{\Delta\mu}_{bl} & \overline{\Delta\mu}_{cl} \\ \overline{\Delta\mu}_{bh} & \overline{\Delta\mu}_{ch} \end{pmatrix}^{-1}\begin{pmatrix} dD'_l \\ dD'_h \end{pmatrix}=\begin{pmatrix} k_{bl} & k_{bh} \\ k_{cl} & k_{ch} \end{pmatrix}\begin{pmatrix} dD'_l \\ dD'_h \end{pmatrix}, \tag{18}$$

where

$$k_{bl}=\frac{\overline{\Delta\mu_{ch}}}{\overline{\Delta\mu_{bl}}\,\overline{\Delta\mu_{ch}}-\overline{\Delta\mu_{cl}}\,\overline{\Delta\mu_{bh}}}, \tag{19}$$

$$k_{bh}=\frac{-\overline{\Delta\mu_{cl}}}{\overline{\Delta\mu_{bl}}\,\overline{\Delta\mu_{ch}}-\overline{\Delta\mu_{cl}}\,\overline{\Delta\mu_{bh}}}, \tag{20}$$

$$k_{cl}=\frac{-\overline{\Delta\mu_{bh}}}{\overline{\Delta\mu_{bl}}\,\overline{\Delta\mu_{ch}}-\overline{\Delta\mu_{cl}}\,\overline{\Delta\mu_{bh}}}, \tag{21}$$

and

$$k_{ch}=\frac{\overline{\Delta\mu_{bl}}}{\overline{\Delta\mu_{bl}}\,\overline{\Delta\mu_{ch}}-\overline{\Delta\mu_{cl}}\,\overline{\Delta\mu_{bh}}}. \tag{22}$$

Recall that $t_i=f_i(D'_l,D'_h)$, where $i=b,c$; hence $dt_i=(\partial t_i/\partial D'_l)\cdot dD'_l+(\partial t_i/\partial D'_h)\cdot dD'_h$. But from Eq. (18), $(\partial t_i/\partial D'_l)=k_{il}$ and $(\partial t_i/\partial D'_h)=k_{ih}$, therefore, the variance of t_i, namely $\sigma^2_{t_i}$, can be expressed as

$$\sigma^2_{t_i}=(\partial t_i/\partial D'_l)^2\cdot\sigma^2_{D'_l}+(\partial t_i/\partial D'_h)^2\cdot\sigma^2_{D'_h}=k^2_{il}\cdot\sigma^2_{D'_l}+k^2_{ih}\cdot\sigma^2_{D'_h};\quad i=b,c. \tag{23}$$

The terms σ_{t_b} and σ_{t_c} represent noise levels in the glandular tissue and calcification subtraction images, respectively. Equation (23) can be rewritten, using Eq. (12), as follows:

$$\sigma^2_{t_i}=\frac{k^2_{il}}{\mathrm{SNR}^2_{S_l}}+\frac{k^2_{ih}}{\mathrm{SNR}^2_{S_h}};\quad i=b,c. \tag{24}$$

The SNR of the subtraction signals, t_b and t_c, can then be expressed as follows:

$$\mathrm{SNR}_{t_i} = \frac{t_i}{\sqrt{\dfrac{k_{il}^2}{\mathrm{SNR}_{S_l}^2} + \dfrac{k_{ih}^2}{\mathrm{SNR}_{S_h}^2}}}; \quad i = b,c. \tag{25}$$

Notice that in the μC subtraction images (t_c) the adipose tissue structures are cancelled out, providing a uniform background signal fluctuating around zero. Thus, the SNR of the μC signal in the subtraction image (SNR_{t_c}) is the same as the CNR.

Since $\mathrm{SNR}_{S_{l,h}}$ is proportional to d [Eq. (14)] and $\mathrm{SNR}_{t_{b,c}}$ is proportional to $\mathrm{SNR}_{S_{l,h}}$ [Eq. (25)], $\mathrm{SNR}_{t_{b,c}}$ is also proportional to d. This results from the fact that the variance of quantum (Poisson) noise fluctuations in the raw (unsubtracted) images is proportional to the number of photons incident on the image pixel area [Eq. (13)]. This seems to imply that systems with larger pixel sizes have the advantage of producing higher SNRs. However, it is important to note that the detectability of an object (μC) is directly proportional to the SNR^2 per pixel summed over all pixels in the object (μC) area rather than in just one pixel.[14] Assuming that the SNR^2 (equal to CNR^2 in the μC subtraction image) is uniform over the object area, the sum of SNR^2 over the object area is equivalent to replacing the pixel area (d^2) with the projected object (μC) area in Eq. (14). For simplicity, the shape of the μCs was assumed to be cubic with a dimension of t_c. This leads to uniform CNRs within the μC, due to the uniform μC thickness, but still reflects the fact that smaller calcifications are also lower in contrast due to shorter attenuating thickness. Thus, the pixel area d^2 was replaced by t_c^2 in all numerical computations in this study. This allows the computed CNRs to be directly used to access and compare the detectability of μCs. During the x-ray detection process, only part of the x-ray energy is converted into fluorescent light in the x-ray scintillator. Although the ratio of x-ray photon energy that is converted to optical light varies slightly with energy, to a good approximation, we can assume that this ratio is constant in the diagnostic energy range (10–120 keV). Thus, in our calculations, the scintillator gain $Q(E)$ is modeled as being proportional to E [i.e., $Q(E) = \alpha E$].

F. Calcification contrast-to-noise and contrast-to-background ratio

A problem in detecting μCs in mammograms is the presence of cluttered tissue structure in the image that constitutes an added ''noise'' component. This component is referred to as the ''tissue structure noise'' for the remainder of the manuscript. The tissue structure noise is intrinsically different from quantum noise. Quantum noise is random and hence follows Poisson statistics. Also, it decreases in size relative to the signal as the exposure level increases, thus potentially improving the detectability of the μCs if no cluttered tissue structure is present in the background. However, the level of tissue structure noise is independent of the exposure level and cannot be improved by increased exposure. The tissue structure noise poses an ultimate limitation for detecting and visualizing μCs in single-energy imaging techniques.

While the level of random noise can be quantified by the standard deviation of fluctuating signals in a region of uniform exposure; the level of tissue structure noise cannot be easily quantified since the degree of obscurity varies greatly with the pattern of the tissue structure and its relative position with respect to the μC. Despite these differences, it may be instructive to use the range of signal or contrast variations due to tissue structures to represent the level of tissue structure noise, and compute an image characteristic referred to as the calcification contrast-to-background ratio (CCBR). As an analogy to the calcification contrast-to-noise ratio (CCNR), the CCBR is computed as the ratio of the calcification contrast to the signal range or the contrast of the background tissue structure. Assuming that for a breast of thickness T, the background area consists of 50% adipose and 50% glandular tissue. The background signal, S_B, can be computed using Eq. (2) as

$$S_B = \int dE \cdot R \cdot t_c^2 \cdot \Phi(E) \cdot e^{-(0.5\mu_a(E) + 0.5\mu_b(E))T} \cdot A(E) \cdot Q(E). \tag{26}$$

The noise in S_B can be computed using Eq. (13) as

$$\sigma = \left(\int dE \cdot R \cdot t_c^2 \cdot \Phi(E) \cdot e^{-(0.5\mu_a(E) + 0.5\mu_b(E))T} \cdot A(E) \cdot Q^2(E) \right)^{1/2}. \tag{27}$$

Now assume that there also exists an overlapping tissue structure in which the tissue composition varied from 50% adipose and 50% glandular to 25% adipose and 75% glandular. The signal for 25% adipose and 75% glandular tissue composition of thickness T can be expressed as

$$S_T = \int dE \cdot R \cdot t_c^2 \cdot \Phi(E) \cdot e^{-(0.25\mu_a(E) + 0.75\mu_b(E))T} \cdot A(E) \cdot Q(E). \tag{28}$$

Thus, the signal range or contrast of the tissue structure due to tissue composition variation (TC) can be computed as the difference between S_B and S_T, i.e., $TC = S_B - S_T$. This can be used to quantify the level of the ''tissue structure noise'' for the previously described tissue structure.

Assuming that a μC replaces a cubic volume of 50% adipose and 50% glandular background tissue of dimension t_c, the image signal over the μC can be computed as

$$S_C = \int dE \cdot R \cdot t_c^2 \cdot \Phi(E) \cdot e^{-(0.5\mu_a(E) + 0.5\mu_b(E))(T - t_c) - \mu_c(E)t_c} \cdot A(E) \cdot Q(E). \tag{29}$$

The difference signal for this μC can then be computed as $CC = S_B - S_C$. From our earlier definitions, the calcification contrast-to-noise ratio, $\mathrm{CCNR} = CC/\sigma$, and the calcification contrast-to-background ratio, $\mathrm{CCBR} = CC/TC$. The range of

tissue composition between 50% adipose and 50% glandular to 25% adipose and 75% glandular tissue compositions used in this discussion was arbitrarily chosen as only the general behaviors of CCNR and CCBR were studied.

III. MATERIALS AND METHODS

In order to compute the calcification SNR in the subtraction images [Eq. (25)], it was necessary to compute the k_{ij} coefficients [Eqs. (19)–(22)] and the SNR for low- and high-energy images [Eq. (14)]. In addition, the imaging parameters, namely the x-ray spectra, attenuation coefficients, and detector absorption ratios, were determined from published data for the energy ranges studied. The methods for these computations are described and discussed in the following sections.

A. X-ray photon spectra

In this study, both mammographic and general radiographic x-ray spectra were used. The published mammographic x-ray spectra[15] used were for x rays generated with a molybdenum target and a 30 μm thick molybdenum filter (Mo/Mo) at 25, 30, 35, 40, 45, and 50 kVp; and for a tungsten target and lanthanum filter (W/La) at 50 kVp. The published general radiography x-ray spectra[16] used were for x rays generated with a tungsten target and a 2.0 mm thick aluminum filter at 50–90 kVp, and with a tungsten target and a 0.25 mm thick copper filter at 100–140 kVp. All published spectra data were normalized and converted into the photon fluence spectrum, $\Phi(E)$, with units of photons/cm^2 C/kg at a resolution of 1 keV.

Note that the mammographic spectra data used were measured for the older generation of mammographic tubes with glass windows. It has been suggested that x rays generated by these types of tubes are subject to greater beam hardening than those generated by the more modern tubes that uses beryllium windows.[17] Mammographic spectra for the latter type of tubes are currently being measured and compiled for public release.

B. Photon absorption ratio for scintillators

Scintillators (e.g., cesium iodide, sodium iodide) are commonly used in x-ray detectors to convert x rays into optical light. Although x-ray detectors using photoconductor materials (e.g., selenium) have been developed and commercialized, most digital mammographic systems rely on scintillators for x-ray detection. In this paper, we consider two scintillators commonly used in digital mammography systems: terbium-doped gadolinium oxysulfide (Gd_2O_2S:Tb) and thallium-doped cesium iodide (CsI:Tl). Usually, Gd_2O_2S:Tb is used with both charge-coupled devices (CCD) and amorphous silicon (aSi:H) flat-panel-based detectors while CsI:Tl (usually grown as column structures directly on the photodiode array) is only used with aSi:H flat-panel detectors. The densities of Gd_2O_2S:Tb and crystalline CsI:Tl are 7.34 and 4.51 g/cm^3, respectively, while the density of CsI:Tl grown as a column structure will be less than its density in crystalline form. The exact density and thickness of the CsI layer used in flat-panel detectors vary from system to system and are often withheld as proprietary information by the manufacturers. However, for the purposes of our calculations the relevant value is the product of density and thickness. A scintillator "thickness" of 34 mg/cm^2 for Gd_2O_2S:Tb and 45 mg/cm^2 for CsI:Tl were used in this numerical study. The Gd_2O_2S:Tb thickness used is similar to that of Lanex Fine screens, whereas the CsI:Tl thickness approximates that of commercially available CsI-based flat-panel mammography systems.

The x-ray absorption ratios, $A(E)$, were calculated for photon energies between 10 and 140 keV at a resolution of 1 keV, using linear-attenuation coefficients interpolated from data published by NIST[18] as follows:

$$A(E) = 1 - e^{-\mu_s(E)t_s}, \tag{30}$$

where, $\mu_s(E)$ and t_s are the energy-dependent linear attenuation coefficient (l/cm) and scintillator thickness (cm), respectively.

C. X-ray attenuation coefficients

The elemental compositions of adipose and glandular breast tissue,[19] the calcifications ($CaCO_3$), and the scintillators (Gd_2O_2S:Tb and CsI:Tl) were used to calculate the mass-attenuation coefficients (μ/ρ) using data published by NIST.[18] Since the published attenuation coefficients are provided only for a limited number of discrete photon energies, a log-linear interpolation was used to compute the coefficients for intermediate energies at 1 keV intervals. The interpolation was performed using the following exponential model relating the coefficient to the photon energy:

$$\left(\frac{\mu}{\rho}\right) = \kappa . E^{\beta}. \tag{31}$$

Taking the logarithms, Eq. (31) can be converted into a linear equation. Using published attenuation coefficients $(\mu/\rho)_1$ and $(\mu/\rho)_2$ at two known consecutive energies of E_1 and E_2, the linear coefficients ($\ln\kappa$ and β) were determined as follows:

$$\beta = \frac{\ln\left(\frac{\mu}{\rho}\right)_2 - \ln\left(\frac{\mu}{\rho}\right)_1}{\ln E_2 - \ln E_1}, \tag{32}$$

and

$$\ln\kappa = \frac{\ln\left(\frac{\mu}{\rho}\right)_1 \cdot \ln E_2 - \ln\left(\frac{\mu}{\rho}\right)_2 \cdot \ln E_1}{\ln E_2 - \ln E_1}. \tag{33}$$

Substituting the $\ln\kappa$ and β values from above in Eq. (31), (μ/ρ) was then computed for intermediate energies between E_1 and E_2 at 1 keV resolution. The interpolated mass-attenuation coefficient values (μ/ρ) were then multiplied by the density (ρ) of the appropriate material to obtain the linear attenuation coefficients (μ). The density values used for the materials were obtained from published data[18,19] and are listed in Table I.

TABLE I. Materials and their densities used in the numerical computations.

Material	Density (g/cm^3)
$CaCO_3$	2.93
Gd_2O_2S:Tb	7.34
CsI:Tl	4.51
Adipose tissue	0.93
Glandular tissue	1.04

D. X-ray exposure considerations

The skin-entrance exposure for mammography can vary from $(0.258-25.8)\times10^{-4}$ C/kg (0.1–10 R), depending upon the x-ray technique and imaging device.[20–22] Typical mammographic x-ray techniques can produce a detector exposure of $(2.58-3.10)\times10^{-4}$ C/kg (1000–1200 mR) without the breast in the field. In dual-energy imaging the total exposure (unattenuated at the detector) is the sum of the individual low- and high-energy exposures. To compare the dual-energy technique with the single-energy technique in a normalized manner, the total exposure (unattenuated at the input of the detector) of dual-energy image acquisition was kept at 2.58×10^{-4} C/kg (1000 mR). Such a normalization allows the dual-energy and single-energy techniques to be compared for the same x-ray output or skin-entrance exposure. However, the risk to the patient in x-ray mammography is often evaluated by the "mean glandular dose."[19–21] For simplicity, we have computed the calcification SNR by normalizing the total unattenuated detector exposure to be 1000 mR. The results can be easily extrapolated to other exposure values or normalized to the mean-glandular dose, as will be discussed in Sec. IV F. The optimal distribution of the exposure between the low- and high-energy images was studied by computing the noise levels in the subtraction image signals as a function of the "low-energy exposure ratio," defined as the ratio of the low-energy exposure to the total exposure.

E. Noise level in the single-energy image signals

As discussed in Sec. II F, the CCNR and CCBR ratios were computed to represent the level of tissue structure noise in the single-energy images. For a 250 μm size μC in a 5 cm thick breast, the CCNR and CCBR were calculated using 50% adipose and 50% glandular tissue composition as the background and its difference from 25% adipose and 75% glandular tissue composition as the contrast due to tissue structure.

F. Noise level in the dual-energy subtraction image signals

A key indicator of image quantity is the image noise level. The noise level in the dual-energy μC image signal, σ_{t_c}, was calculated for various low and high-energy spectral combinations, breast thicknesses, tissue compositions, μC sizes, and low-energy exposure ratios. The breast thickness was varied from 3.5 to 7 cm; the tissue composition varied from 0% glandular (100% adipose) to 100% glandular (0% adipose); the low-energy exposure ratio varied from 0 to 1 while keeping the total unattenuated detector exposure at 1000 mR.

For a given combination of breast thickness, tissue composition, μC size, and low- and high-energy input spectra, the image signals (S_l and S_h) and their associated noise levels for unsubtracted images were calculated using Eqs. (3) and (13), respectively. The average difference-attenuation coefficients ($\overline{\Delta\mu_{ij}}$) were determined with Eq. (16) and then used with Eqs. (19)–(22) to compute k_{ij} values as the inverse matrix of $\overline{\Delta\mu_{ij}}$. The resulting k_{ij} values, together with the SNR values from Eq. (14), were then used to calculate the noise levels in the μC subtraction signals (σ_{t_c}) using Eq. (24). The noise fluctuations in the glandular tissue thickness signals, σ_{t_b}, can be determined using Eq. (24). However, such computations were not part of this study. The procedure to investigate the calcification SNRs for various imaging parameter values (μC size, low- and high-energy kVp values, tissue composition, and breast thickness) in dual-energy subtraction imaging is outlined below.

(I) Assume a compressed breast thickness of 5 cm, 50% adipose and 50% glandular tissue composition, and low-/high-energy input spectra at 25/50 kVp. The noise level in the dual-energy μC image signal, σ_{t_c}, was then computed as a function of the low-energy exposure ratio to determine the minimum μC size that would yield an acceptable SNR (3 or higher).[23]

(II) For a 5 cm thick breast, 50% adipose and 50% glandular tissue composition, and a 250 μm μC size (from step I), the high-energy spectrum was varied from 30 to 50 kVp while keeping the low-energy spectrum fixed at 25 kVp. σ_{t_c} was computed as a function of the low-energy exposure ratio for various kVp combinations to determine the optimal kVp combination.

(III) Using the optimal kVp combination of 25/50 kVp (from step II), a 250 μm μC size, and 50% adipose and 50% glandular tissue composition, σ_{t_c} was computed as a function of the low-energy exposure ratio for various compressed breast thickness ranging from 3.5 to 7 cm.

(IV) Finally, for a 5 cm thick breast, a 250 μm μC size, and a kVp combination of 25/50 kVp, σ_{t_c} was computed as a function of the low-energy exposure ratio for various tissue compositions that varied from 0% glandular (100% adipose) to 100% glandular (0% adipose).

The optimal exposure ratio was determined as the ratio with which σ_{t_c} was at a minimum. The variations of the optimal low-energy exposure ratio with various imaging factors were studied.

IV. RESULTS AND DISCUSSION

A. Photon absorption ratios

The x-ray absorption ratios (see Sec. III C) for a 34 mg/cm^2 thick Gd_2O_2S:Tb scintillator and a 45 mg/cm^2 thick CsI:Tl scintillator are shown in Fig. 2. The curves are very similar from 10 to ~33 keV. Above the k edges of CsI at 33.2 and 36 keV, its absorption ratio increases significantly

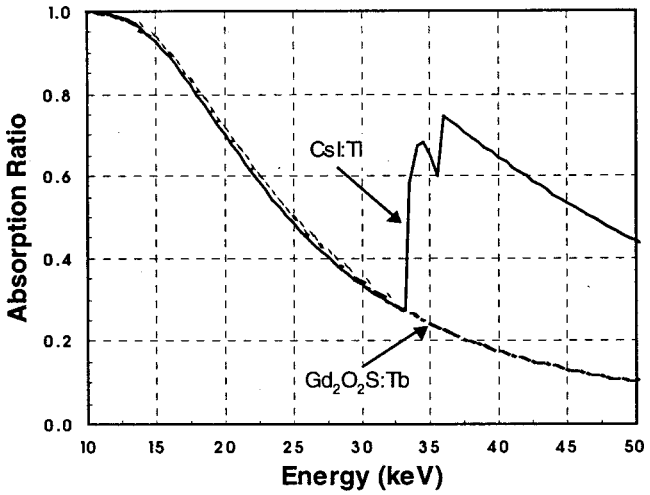

FIG. 2. A plot showing the absorption ratios for a 46 μm thick Gd_2O_2S:Tb scintillator and a 100 μm thick CsI:Tl scintillator. The *k* edges of a CsI:Tl scintillator are seen at 33.2 and 36 keV, resulting in a higher absorption ratio. The *k* edge for Gd_2O_2S:Tb lies at 50.2 keV (just above the plotted energy range).

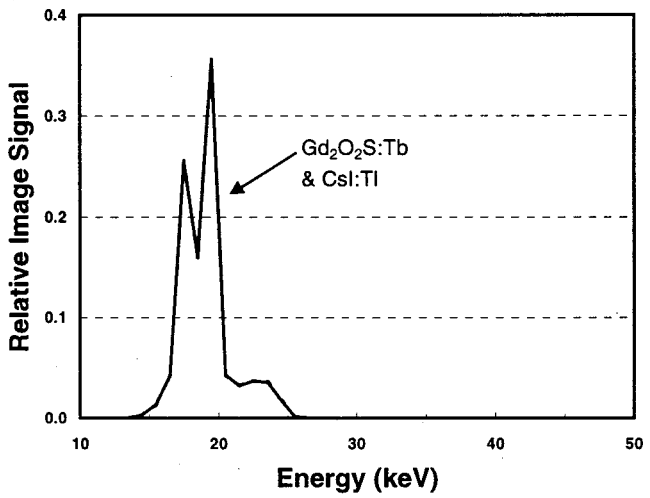

FIG. 3. Plots showing the computed 25 kVp Mo/Mo x-ray spectra for the Gd_2O_2S:Tb and CsI:Tl scintillators. The characteristic x-ray lines of Mo are seen at 17.4 and 19.8 keV. The total signal in each spectrum is normalized to unity. The spectra for both scintillators are identical because their absorption ratios are similar for photon energies below 33 keV (see Fig. 2).

and exceeds that of Gd_2O_2S. This results in higher overall detection efficiency for CsI than that for Gd_2O_2S for x rays generated with a kVp above the *k*-edge energies of CsI. This higher absorption ratio for the CsI scintillator results in higher values of $SNR_{S_{h,l}}$ and thus a decrease in the σ_{t_c} when compared with images acquired with the Gd_2O_2S scintillator above ~33 keV.

B. X-ray source spectra

The x-ray source spectra (see Sec. III A) generated with 25 kVp Mo/Mo, 50 kVp Mo/Mo, and 50 kVp W/La (where the Mo/Mo and W/La refer to the target/filter combinations) and attenuated by 5 cm thick breast with 50% adipose and 50% glandular tissue composition, are plotted in Figs. 3, 4, and 5, respectively. The total signal in the computed spectra are normalized to unity to compare the spectral shapes. Figures 3–5 illustrate the spectral differences between the low- and high-energy x-ray spectra. The *k*-edge absorption by CsI improves its detection efficiency for x rays generated at kVp values above its *k*-edge energies (>33 keV). This would not be an advantage for the x-ray spectra used in regular (single-energy) digital mammography procedures, since the x rays are typically generated at kVp values below the CsI *k*-edge energies. However, the greater absorption ratio of CsI above its *k* edges represents a significant improvement for dual-energy subtraction imaging since CsI yields a higher detector efficiency for the high-energy spectrum.

Figures 3 and 4 clearly show the characteristic x-ray lines of Mo at 17.4 and 19.8 keV. Since the absorption ratio for the two scintillators are similar below ~33 keV (Fig. 2), the detected signal spectra for 25 kVp Mo/Mo should be similar for both scintillators, as indicated by Fig. 3. The bremsstrahlung emission above 20 keV in the 50 kVp Mo/Mo spectrum is seen in Fig. 4. Above the CsI *k*-edge energies, the spectrum detected by CsI shows a higher intensity over the spectrum detected by Gd_2O_2S (see Figs. 4 and 5). The drop around 39 keV in the 50 kVp W/La spectra (Fig. 5) is due to *k*-edge absorption by the La filter. Combining the *k*-edge absorption by the La filter and then by the CsI scintillator, a more peaked spectrum is generated, leading to better energy separation for dual-energy subtraction imaging than the 50 kVp Mo/Mo spectrum detected by CsI.

C. CCNR and CCBR in the unsubtracted images

The CCNR and CCBR (see Secs. II F and III E) are plotted in Fig. 6 as a function of the x-ray spectrum from 25 to 140 kVp. The CCBRs were found to be significantly lower

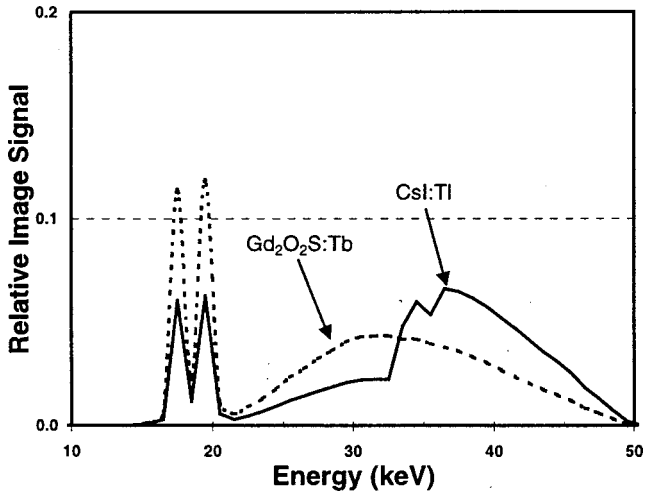

FIG. 4. Plots showing the computed 50 kVp Mo/Mo x-ray spectrum for the Gd_2O_2S:Tb and CsI:Tl scintillators. The total signal in each spectrum is normalized to unity. In addition to the characteristic x-ray lines of Mo below 20 keV, bremsstrahlung emission is seen at higher energies. The bump-like structure seen in the CsI spectrum around 35 keV is due to its higher absorption ratio.

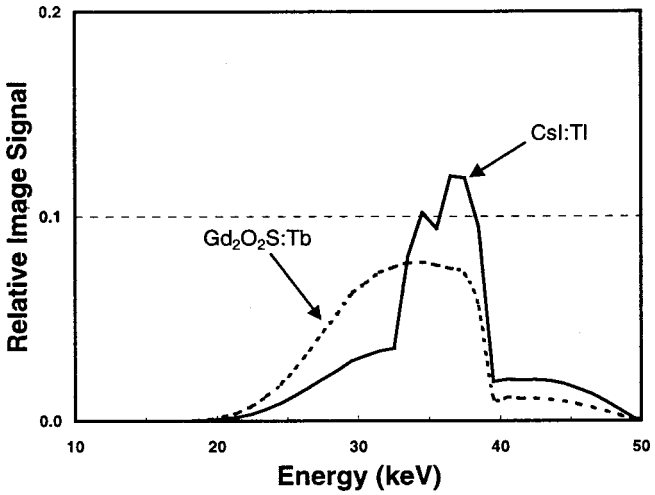

FIG. 5. Plots showing the computed 50 kVp W/La x-ray spectrum for the Gd_2O_2S:Tb and CsI:Tl scintillators. The total signal in each spectrum is normalized to unity. The drop around 39 keV is due to *k*-edge absorption by the La filter. Combining the increased *k*-edge absorption by the CsI scintillator and the La filter attenuation at the source, a more peaked spectrum is generated for the CsI scintillator.

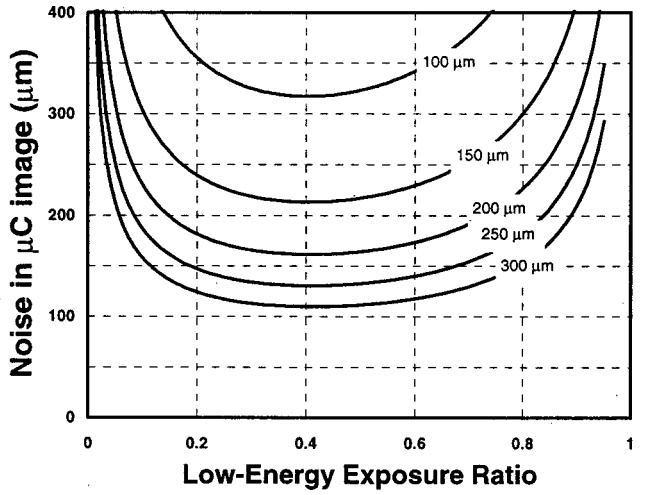

FIG. 7. Plots of the μC image noise (σ_{t_c}) as a function of the low-energy exposure ratio for various sizes of μCs using the Gd_2O_2S:Tb scintillator; assuming a 5 cm thick breast of 50% adipose and 50% glandular tissue composition and 25/50 (Mo/Mo) low/high kVp spectra. Curves are shown for the μC size ranging from 100 to 300 μm in increments of 50 μm.

than the CCNRs, indicating that in single-energy imaging, the detection of μCs can be obscured (difficult to visualize) by the presence of tissue structures, even though the CCNRs may be sufficiently high for detection over a uniform background. In dual-energy subtraction imaging, the tissue structures are cancelled out, or at least significantly reduced, leading to a much higher value for the CCBR. The benefit of dual-energy imaging is to eliminate or greatly reduce the background tissue structures so that they do not obscure and limit the detection and visualization of μCs. However, the drawback of the dual-energy subtraction technique is a decrease of CCNR due to a noise increase from subtraction processing, as discussed in Sec. II E. One major task in designing and testing the dual-energy subtraction imaging technique is to ensure that the CCNR in the subtracted μC images remains sufficiently high for detecting μCs.

As the kVp increased, both the CCNR and CCBR gradually decreased. The steady decrease of CCNR and CCBR indicates that, even though the use of higher kVp x rays tends to reduce the background tissue structure, it also causes the calcification contrast to decrease; resulting in only a slight decrease of the CCBR with kVp. The sudden drop of CCNR at 50 kVp (Fig. 6) is due to the change of target/filter combination from Mo/Mo to W/Al at 50 kVp. Notice that the CCNR was computed by summing the CNR over the μC area. Thus, they could increase with the size of the μC as well as the total exposure used. On the other hand, the CCBR is independent of the exposure and the μC size used.

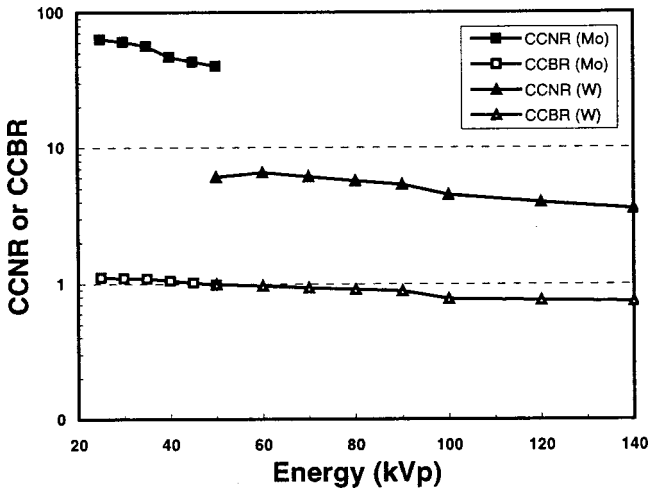

FIG. 6. The plots of the calcification contrast-to-noise ratio, CCNR, and the calcification background-to-noise ratio, CCBR, for energies ranging from 25 to 140 kVp. Target/filter combinations of Mo/Mo, W/Al, and W/Cu were used between 25–50, 50–90, and 100–140 kVp, respectively. The Mo and W labels in the figure represent spectra generated with a molybdenum and a tungsten target, respectively. Note that the 50 kVp calculations were performed with both the Mo and the W targets.

D. Noise level in the microcalcification images

1. Impact of microcalcification size

The noise in the μC image, σ_{t_c}, was calculated as a function of the low-energy exposure ratio, for various μC sizes (100–300 μm) using 25 and 50 kVp (Mo/Mo), and assuming a 50% adipose and 50% glandular tissue composition and a breast thickness of 5 cm. These results are plotted for Gd_2O_2S and CsI scintillators in Figs. 7 and 8, respectively. It has long been recognized that, for the detection of a μC, the object SNR must exceed some minimum value SNR_{min}.[23] In this study we adopt a threshold value of 3 for SNR_{min}.[23] Figure 7 shows that with the Gd_2O_2S scintillator a SNR of 3 is achieved for a μC size of $\sim$300 μm ($\sigma_{t_c} \sim 110\,\mu$m), whereas with the CsI scintillator, as seen in Fig. 8, a SNR of 3 is achieved for a μC size of $\sim$250 μm ($\sigma_{t_c} \sim 80\,\mu$m). The use of the CsI scintillator resulted in a higher SNR (or lower σ_{t_c} values) for all μC sizes. This can be attributed to the higher x-ray absorption ratio of the CsI scintillator above its

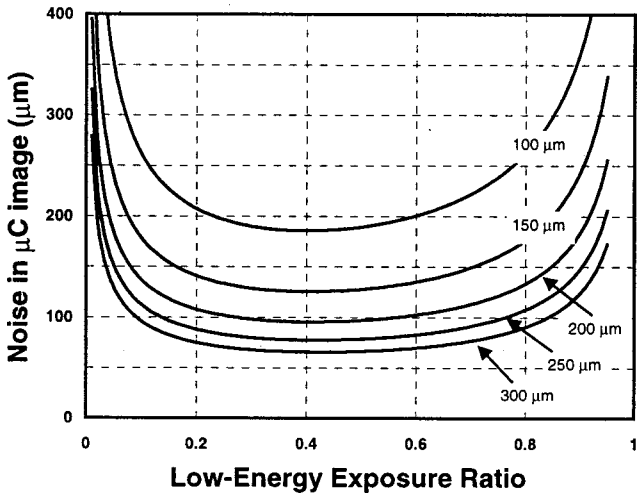

FIG. 8. Plots of the μC image noise (σ_{t_c}) as a function of the low-energy exposure ratio for various sizes of μCs using the CsI:Tl scintillator; assuming a 5 cm thick breast of 50% adipose and 50% glandular tissue composition and 25/50 (Mo/Mo) low/high kVp spectra. Curves are shown for the μC size ranging from 100 to 300 μm in increments of 50 μm.

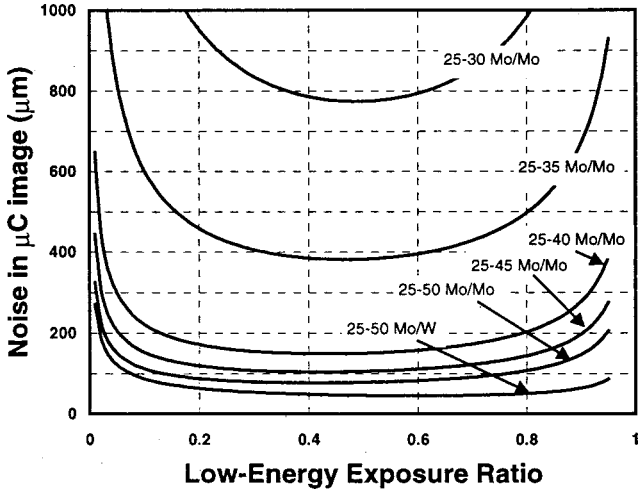

FIG. 9. Plots of μC image noise (σ_{t_c}) as a function of the low-energy exposure ratio for various combinations of energy spectra using the CsI:Tl scintillator; assuming a 5 cm thick breast of 50% adipose and 50% glandular tissue composition and a μC size of 250 μm.

k-edge energies (Fig. 2). Thus, a 250 μm μC size was used in all subsequent computations, as it may be considered as the minimum detectable μC size in dual-energy imaging.

A study of controlled *in vitro* studies of breast μC detectability with a conventional screen film gave a minimum detectable μC size of ~290 μm.[24] Dual-energy mammography utilizing computed radiography yielded a minimum detectable μC size of ~470 μm for $SNR_{min}=5$ (or 350 μm for $SNR_{min}=3$).[7] Other numerical calculations with an ideal detector and monoenergetic x rays at 19 and 68 keV predict the detection of a 200 μm cubic calcification with $SNR_{min}=5$.[2] Our results, derived under idealized conditions (no detector noise), indicate a threshold size of ~250 μm for $SNR_{min}=3$. The differences in the predicted minimum detectable μC size seems to reflect the differences in the quality of the detector used (scintillator versus ionization chamber versus storage phosphor), the x-ray spectra used (mono- versus polyenergetic) as well as the SNR threshold value used (3 vs 5). At first glance, the threshold μC size with dual-energy imaging does not appear to be very different than those from conventional techniques. However, the advantage of dual-energy imaging is in its ability to suppress structure noise. While the μC threshold size with conventional techniques vary across the images and increase in those regions with a higher structure noise, the threshold size with dual-energy imaging stays more uniform across the image due to the suppression of structure noise. Further experiments and studies after a full implementation of a dual-energy imaging system will be needed to fairly evaluate threshold μC detectability and address the clinical relevance of dual-energy mammography.

2. Impact of spectral energy separation

Using a 250 μm μC size, σ_{t_c}, was computed for various kVp combinations: the low-energy spectrum fixed at 25 kVp (Mo/Mo) and high-energy spectrum at 30, 35, 40, 45, or 50 kVp (Mo/Mo). At 50 kVp, the W/La target/filter combination was also used. In Fig. 9, σ_{t_c} is plotted as a function of the low-energy exposure ratio for various kVp combinations for the CsI scintillator. The plots show that as the energy separation widened, the μC image noise decreased. Similar results were observed for the Gd_2O_2S scintillator, but with slightly higher noise levels due to lower x-ray absorption with the Gd_2O_2S scintillator. The combination of 25 kVp (Mo/Mo) and 50 kVp (W/La) x-ray spectra, labeled 25–50 Mo/W in Fig. 9, resulted in the lowest σ_{t_c}.

Earlier works, assuming monoenergetic x rays, have suggested that 19 and ~70 keV are the optimal low and high energies for dual-energy imaging.[2,6] Our calculations are based on polyenergetic mammographic spectra and incorporate clinically relevant considerations. A molybdenum target/filter was used in our calculations since they are used widely in modern mammography units and have been shown to provide better radiographic contrast than tungsten targets.[25,26] The low-energy spectrum was fixed at 25 kVp because lower kVp values are seldom used in clinical procedures. Calculations regarding the high-energy beam stopped at 50 kVp because most mammography units do not operate above it. While our aim in this paper is to evaluate and optimize the technique for dual-energy imaging, standard clinical practices and practical considerations were maintained. In subsequent calculations, 25 kVp (Mo/Mo) and 50 kVp (Mo/Mo) were used for the low- and high-energy x-ray spectra, respectively.

3. Impact of breast thickness

In Fig. 10, σ_{t_c} is plotted as a function of the low-energy exposure ratio for a compressed breast thickness between 3.5 and 7 cm using CsI as the scintillator. σ_{t_c} increased with the breast thickness by a factor of ~2 over the range of breast thickness considered. As the breast thickness increases, the

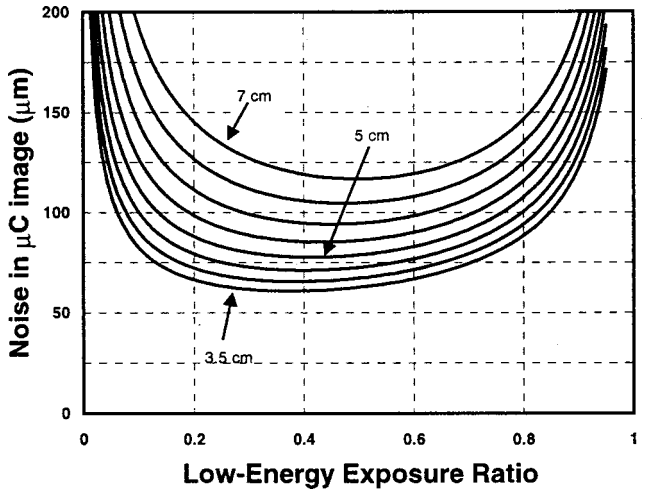

FIG. 10. Plots of μC image noise (σ_{t_c}) as a function of the low-energy exposure ratio for various breast thicknesses using the CsI:Tl scintillator; assuming 50% adipose and 50% glandular tissue composition, a μC size of 250 μm, and 25/50 (Mo/Mo) kVp spectra. Curves are shown for breast thicknesses ranging from 3.5 to 7 cm in increments of 0.5 cm.

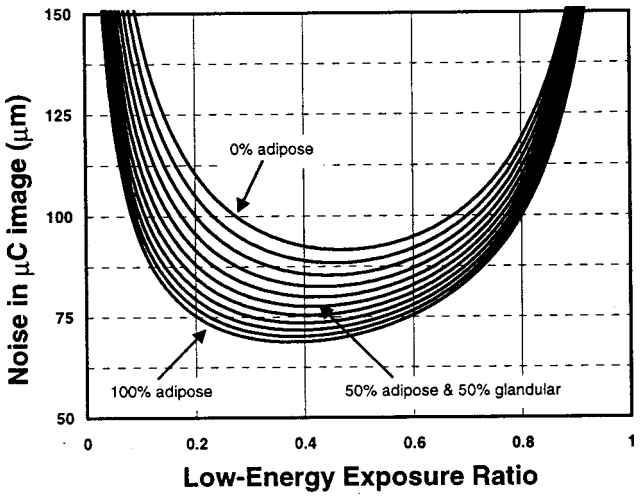

FIG. 11. Plots of μC image noise (σ_{t_c}) as a function of the low-energy exposure ratio for various adipose/glandular tissue compositions using the CsI:Tl scintillator; assuming a 5 cm thick breast, a 250 μm μC size, and 25/50 (Mo/Mo) kVp spectra. Curves are shown for compositions varying from 0% adipose (100% glandular) to 100% adipose (0% glandular) in increments of 10% adipose.

x-ray photons have to travel through more attenuating material. Thus, for a fixed unattenuated detector exposure, a thicker breast decreases the number of x-ray photons arriving at the detector. With fewer photons detected, the μC image noise increases in the subtracted image with thicker breasts (see Fig. 10). Similar results were observed for the Gd_2O_2S scintillator, but with slightly higher noise levels due to lower x-ray absorption in the Gd_2O_2S scintillator for higher-energy x rays.

4. Impact of tissue composition

In Fig. 11, σ_{t_c} is plotted as a function of the low-energy exposure ratio for various tissue compositions using CsI as the scintillator. σ_{t_c} varies by as much as ~50% as the composition varies from 0% glandular to 100% glandular. The density of glandular tissue (1.04 g/cm^3) is greater than the density for adipose tissue (0.93 g/cm^3). Hence, for a fixed breast thickness, the breast density increases with the glandular tissue content, leading to higher x-ray attenuation. As discussed in the previous paragraph, higher attenuation decreases the number of detected photons and hence leads to an increase in the μC image noise for the same exposure. Therefore, as seen in Fig. 11, the μC image noise increases with the glandular tissue content. Similar results were observed for the Gd_2O_2S scintillator, but with slightly higher noise levels due to lower x-ray absorption in the Gd_2O_2S scintillator for higher-energy x rays.

E. Optimal low-energy exposure ratio

The optimal low-energy exposure ratio is defined as the one that minimizes the level of the μC image noise (σ_{t_c}). The ratio may be a function of the μC size, low-/high-energy spectral combination, tissue composition, and breast thickness. The optimal low-energy exposure ratio can be determined from the plots in Figs. 8–11. The range of optimal low-energy exposure ratios refers to the σ_{t_c} values within 10% of the minimum. The optimal range varied with tissue composition from 0.27–0.68 for 0% adipose tissue to 0.19–0.61 for 100% adipose tissue. The optimal range varied with the compressed breast thickness from 0.19–0.61 for a 3.5 cm breast to 0.29–0.71 for a 7 cm breast, assuming a 50% adipose and 50% glandular tissue composition. Finally, the optimal range varied with the μC size from 0.21–0.62 for 100 μm to 0.22–0.65 for 300 μm, assuming a 50% adipose and 50% glandular tissue composition for a 5 cm thick breast. Based on the overlap of these ranges, we have concluded that for low-energy exposure ratios between 0.29 and 0.61, the estimated σ_{t_c} values would be within 10% of the minimum values for various tissue compositions, breast thicknesses, and μC sizes.

This leads to an important consideration for practical implementation: the total exposure can be distributed over a wide range between the low- and high-energy images over various breast thicknesses while maintaining σ_{t_c} values within 10% of its minimum. The low-/high-energy exposure distribution can be varied (from 30%/70% to 60%/40%) without significantly affecting the results. This greatly simplifies the practical implementation of dual-energy μC imaging techniques. These observations are evident from the (flat) shapes of the curves in Figs. 8–11.

F. Dosimetric considerations

Another consideration for dual-energy μC imaging is the total mean-glandular tissue dose. For a given exposure, the exposure-to-dose conversion factors can be used to convert the skin entrance exposure measurement into the mean-glandular tissue dose.[19,21,27] By extrapolating published data, it was determined that using a 50 kVp spectrum would increase the conversion factor by 50% as compared to using a 25 kVp spectrum. This would effectively increase the total

mean-glandular tissue dose in dual-energy image acquisition if the total detector exposure or entrance skin exposure is kept at the same level of a regular mammographic image. For example, a 2.58×10^{-4} C/kg (1000 mR) exposure at the skin entrance of the breast split evenly between 25 and 50 kVp images would result in a total mean-glandular tissue dose of ~1.55 mGy; whereas the same 2.58×10^{-4} C/kg (1000 mR) exposure made at 25 kVp would result in a dose of ~1.23 mGy. Therefore, dual-energy image acquisition at 25/50 kVp results in an overall increase in the mean-glandular tissue dose by a factor of 1.25 if the total exposure is kept the same as that of a 25 kVp mammogram. Thus, in order to compensate for this increase in dose, the total exposure for 25/50 kVp dual-energy imaging would need to be reduced to approximately 80%, i.e., 2.06×10^{-4} C/kg (800 mR), to keep the mean-glandular dose the same for comparison. The implications are an approximate 10% increase in all noise levels computed, including those for the μC image signal, σ_{t_c}. Similar but lower noise increases should be observed for other low/high kVp combinations used in this study since the increase in conversion factors for kVp values lower than 50 should be smaller. Thus, the noise increase from normalization to a fixed mid-glandular dose is small and should not significantly affect the results or conclusions of this study based on a fixed total detector exposure of 2.58×10^{-4} C/kg (1000 mR).

V. CONCLUSIONS AND SUMMARY

The CsI:Tl scintillator has a higher absorption ratio than Gd_2O_2S:Tb at energies above 33.2 keV (Fig. 2) due to *k*-edge absorption at 33.2 and 36 keV. Since more photons are detected for a given exposure by CsI, the dual-energy calcification images obtained with CsI scintillators have lower noise (higher SNR) compared to those obtained with Gd_2O_2S scintillators. For a 5 cm thick breast composed of 50% adipose and 50% glandular tissue, a μC size of 250 μm yielded an object CNR of approximately 3:1 with the CsI scintillator and approximately 2:1 with the Gd_2O_2S scintillator (Figs. 7 and 8) with a 25/50 kVp low-/high-energy spectra. Hence, CsI is better suited for dual-energy subtraction mammography than the Gd_2O_2S scintillator.

The CCNR and CCBR were calculated for single-energy x rays with kVp ranging from 25 to 140 (Fig. 6). Although tissue contrast can be reduced by imaging at a higher kVp, the calcification contrast also decreases. Thus, for single-energy images, there is no net benefit in switching to a higher kVp for the detection or visualization of μCs. In fact, the μC contrast decreases at a slightly higher rate relative to tissue contrast. The results showed that the limitations of μC visibility by the tissue structure noise must be addressed by methods designed to eliminate or reduce background tissue structure, including but not limited to dual-energy subtraction.

It was also shown that the μC image noise (σ_{t_c}) decreased as the spectral energy separation increased (Fig. 9). Using 25 kVp Mo/Mo and 50 kVp W/La spectra resulted in the lowest noise. Although Mo/Rh (rhodium) dual-target tubes are available, a Mo/W dual-target tube is not currently available; such a tube could provide an advantage for implementation of dual-energy digital mammography.

Simulations were also done to study the effects of the breast thickness (Fig. 10) and tissue composition (Fig. 11). As expected, σ_{t_c} increased as the x-ray attenuation in the breast increased as a result of a thicker breast or a higher glandular tissue content. It was also determined that evenly splitting the exposure between the low- and high-energy images would be sufficient to keep σ_{t_c} within 10% of its minimum value. The low/high exposure can be varied from 30%/70% to 60%/40% without significantly affecting the image quality.

The effects of various imaging parameters to the signal-to-noise in dual-energy mammography have been investigated in this study. A theoretical framework for calculating the calcification CNR in the subtraction images has been developed. We believe that these findings should be of value in guiding the design and implementation of a dual-energy subtraction technique for improved detection and visualization of microcalcifications.

A signal-to-noise analysis, as is done in this study, represents the first step in evaluating the implementation dual-energy imaging. Other issues that influence the practicality of clinical implementation include the development of reliable subtraction algorithms and dual-energy acquisition techniques. The impact of nonuniform detector response and scatter radiation must also be addressed.

ACKNOWLEDGMENTS

This work was supported in part by Research Grant No. DAMD 17-00-1-0316 from the Department of Army Breast Cancer Research Program, Research Grant No. CA51248 from the National Cancer Institute, and a research grant from the Mike Hogg Foundation.

[a]Present address: MeritCare Roger Maris Cancer Center, Fargo, North Dakota 58122.
[b]Author to whom correspondence should be addressed. Department of Imaging Physics, U. of Texas M.D. Anderson Cancer Center, 1515 Holcombe Boulevard, Box 56, Houston, Texas 77030. Phone: 713-745-2835; fax: 713-745-0581; electronic mail: skappadath@mdanderson.org

[1] K. Smigel, "Breast cancer death rates decline for white women," J. Natl. Cancer Inst. (1940-1978) **87**, 173 (1995).
[2] P. C. Johns and M. J. Yaffe, "Theoretical optimization of dual-energy x-ray imaging with applications to mammography," Med. Phys. **12**, 289–296 (1985).
[3] P. C. Johns, D. J. Drost, M. J. Yaffe, and A. Fenster, "Dual-energy mammography: Initial experimental results," Med. Phys. **12**, 297–304 (1985).
[4] D. P. Charkraborty and G. T. Barnes, "An energy sensitive cassette for dual-energy mammography," Med. Phys. **16**, 7–13 (1989).
[5] J. M. Boone, G. S. Shaber, and M. Tecotzky, "Dual-energy mammography: a detector analysis," Med. Phys. **17**, 665–675 (1990).
[6] J. M. Boone, "Color mammography: image generation and receiver operating characteristic evaluation," Invest. Radiol. **26**, 521–527 (1991).
[7] D. S. Brettle and A. R. Cowen, "Dual-energy digital mammography utilizing stimulated phosphor computed radiography," Phys. Med. Biol. **39**, 1989–2004 (1994).
[8] T. Asaga, C. Masuzawa, A. Yoshida, and H. Mattsuura, "Dual-energy subtraction mammography," J. Digit. Imaging **8**, 70–73 (1995).
[9] C. C. Shaw and D. Gur, "Comparison of three different techniques for dual-energy subtraction imaging in digital radiography: A signal-to-noise analysis" J. Digit. Imaging **5**, 262–270 (1992).

[10] F. Kelcz, C. A. Mistretta, and S. J. Riederer, ''Spectral considerations for absorption-edge fluoroscopy,'' Med. Phys. **4**, 26–35 (1977).
[11] D. S. Breitenstein and C. C. Shaw, ''Comparison of three tissue composition measurement techniques using digital mammograms—a signal-to-noise study,'' J. Digit. Imaging **11**(3), 137–150 (1998).
[12] G. T. Barnes, ''Noise analysis of radiographic imaging,'' in *Recent Advances in Digital Imaging*, Proceedings of the 1984 AAPM Summer School, edited by K. Doi, L. Lanzl, and P. J. P. Lin (American Institute of Physics, Woodbury, NY, 1985), pp. 16–38.
[13] A. Macovski, *Medical Imaging Systems* (Prentice–Hall, Englewood Cliffs, NJ, 1983).
[14] R. F. Wagner, ''Decision theory and the detail signal-to-noise ratio of Otto Schade,'' Photograph. Sci. Eng. **22**, 41–45 (1978).
[15] T. R. Fewell and R. E. Shuping, *Handbook of Mammographic X-Ray Spectra*, Rockville, BRH (FDA), 1978.
[16] R. Birch, M. Marshall, and G. M. Ardan, *Catalogue of Spectral Data For Diagnostic X-rays* (The Hospital Physicists' Association, London, 1979).
[17] R. J. Jennings (private communication, 2001).
[18] J. H. Hubbell and S. M. Seltzer, ''Tables of x-ray mass attenuation coefficients and mass energy-absorption coefficients,'' National Institute of Standards and Technology, http://physics.nist/gov/PhysRefData/XrayMassCoef/cover.html, 1996.
[19] R. Hammerstein *et al.*, ''Absorbed dose in mammography,'' Radiology **130**, 485–491 (1979).
[20] H. E. Johns and J. R. Cunningham, *The Physics of Radiology*, 4th ed. (Charles C. Thomas, Springfield, IL, 1983).
[21] L. N. Rothenberg, ''Exposures and doses in mammography,'' in *Syllabus: A Categorical Course in Physics Technical Aspects of Breast Imaging*, edited by A. G. Haus and M. J. Yaffe, 3rd ed. (RSNA, IL, 1994), pp. 113–119.
[22] S. E. Skubic and P. P. Fatouros, ''Absorbed breast dose: dependence on radiographic modality and technique, and breast thickness,'' Radiology **161**, 263–270 (1986).
[23] P. G. J. Barten, *Contrast Sensitivity of the Human Eye and its Effect on Image Quality* (SPIE Optical Engineering, Bellingham, WA, 1999).
[24] E. A. Sickles, ''Mammographic detectability of breast microcalcifications,'' Am. J. Roentgenol., Radium Ther. Nucl. Med. **139**, 913–918 (1982).
[25] A. G. Haus, C. E. Metz, J. T. Chiles, and K. Rossmann, ''The effect of x-ray spectra from molybdenum and tungsten target tubes on image quality in mammography,'' Radiology **118**, 705–709 (1976).
[26] M. J. Yaffe, R. Jennings, R. Fahrig, and T. Fewell, ''X-ray spectral considerations for mammography,'' in Ref. 21, pp. 63–73.
[27] X. Wu, G. T. Barmes, and D. M. Tucker, ''Spectral dependence of glandular tissue dose in screen-film mammography,'' Radiology **179**, 143–148 (1991).